Journal of ELECTRONIC MATERIALS, Vol. 44, No. 9, 2015
DOI: 10.1007/s11664-015-3767-8
© 2015 The Minerals, Metals & Materials Society

CrossMark

Numerical Modeling of SRH and Tunneling Mechanisms in High-Operating-Temperature MWIR HgCdTe Photodetectors

MARCO VALLONE,[1] MARCO MANDURRINO,[1] MICHELE GOANO,[1,2,4] FRANCESCO BERTAZZI,[1,2] GIOVANNI GHIONE,[1] WILHELM SCHIRMACHER,[3] STEFAN HANNA,[3] and HEINRICH FIGGEMEIER[3]

1.—Dipartimento di Elettronica e Telecomunicazioni, Politecnico di Torino, Corso Duca degli Abruzzi 24, 10129 Turin, Italy. 2.— IEIIT-CNR, Politecnico di Torino, Corso Duca degli Abruzzi 24, 10129 Turin, Italy. 3.— AIM Infrarot-Module GmbH, Theresienstraße 2, 74072 Heilbronn, Germany. 4.—e-mail: michele.goano@polito.it

A combined experimental and numerical simulation study is presented on two sets of nominally identical $Hg_{1-x}Cd_xTe$ single-color back-illuminated midwave-infrared *n*-on-*p* photodetectors grown by liquid-phase epitaxy, *p*-doped with Hg vacancies and with Au, respectively. The present numerical model includes a novel formulation for band-to-band tunneling, which overcomes the intrinsic limitations of the classical Kane description without introducing numerical issues typical of other approaches. Our study confirms that adopting *n*-on-*p* architectures, avoiding metal vacancy doping, and reducing the acceptor density in the absorber region are prerequisites for obtaining high-operating-temperature photodetectors. A significant contribution to the dark current in both sets of devices is attributed to impact ionization, crucial to obtain a satisfactory explanation for the measured characteristics also at low to intermediate bias.

Key words: Infrared photodetectors, HgCdTe, tunneling, impact ionization, generation–recombination, numerical simulation

INTRODUCTION

Next-generation infrared (IR) detectors require focal-plane arrays[1–5] designed according to the high-operating-temperature (HOT) concept.[6,7] HOT narrow-gap semiconductor devices operate in nonequilibrium mode such that the carrier densities are held below their equilibrium, near-intrinsic, levels. Since HOT infrared detectors should preserve at 150 K and above the performance characteristics formerly obtained at substantially lower temperatures (80 K to 100 K), a considerable reduction of the dark current is essential to obtain high sensitivity.[8–11]

Two sets of devices, manufactured with the same nominal structure but different *p*-doping technologies, are presented in "Device Fabrication and Experimental Dark Currents" section, and their experimental dark currents are compared and discussed. In "Simulation of the Low Reverse Bias Regime" section, a simulation study of the dark currents demonstrates the favorable effects on Shockley–Read–Hall (SRH) and Auger generation–recombination (GR) rates of avoiding metal-vacancy doping and reducing the acceptor density. "Simulation of the High Reverse Bias Regime" section discusses the significant role of impact ionization (II) and, in one set of examined devices, band-to-band tunneling (BTBT), having applied to graded-composition HgCdTe-based detectors a novel BTBT formulation derived from a description originally conceived for Si-based devices.[12,13]

DEVICE FABRICATION AND EXPERIMENTAL DARK CURRENTS

In this work we compare two sets of $Hg_{1-x}Cd_xTe$ back-illuminated MWIR photodetectors with cutoff wavelength $\lambda_c \approx 5.3\,\mu m$ at $T = 80\,K$, grown by

(Received November 10, 2014; accepted March 25, 2015; published online April 24, 2015)

www.manaraa.com

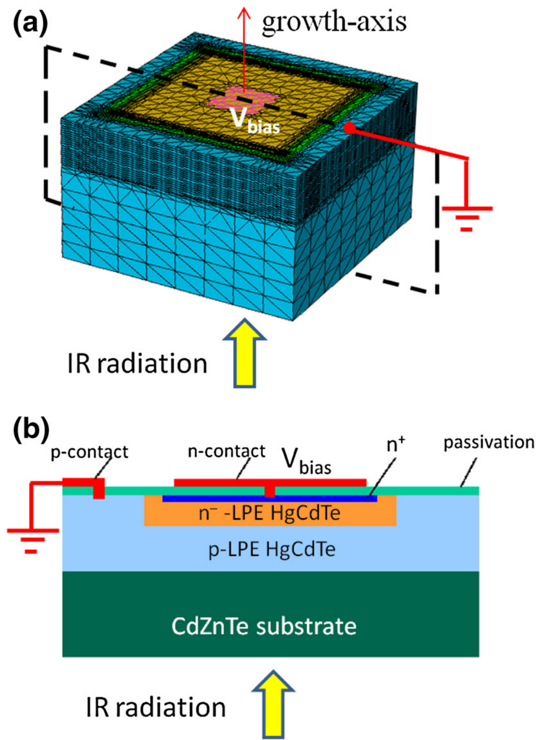

Fig. 1. 3D structure of the single-pixel photodetectors under study (a) and 2D cross-section at the device center (b).

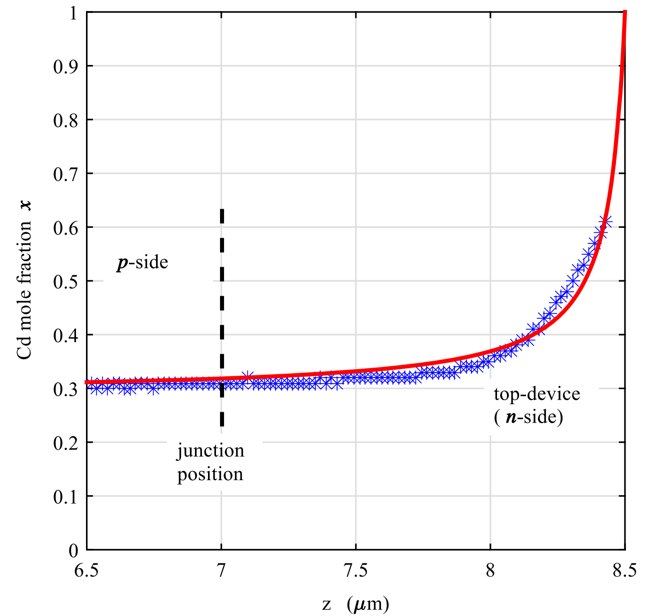

Fig. 2. SIMS profile of the Cd mole fraction x near the surface (blue symbols) and least-squares fit used in the simulations (red solid line). The surface is located at $z = 8.5\,\mu$m; the estimated position of the p–n^- junction is marked with a vertical dashed line (Color figure online).

liquid-phase epitaxy (LPE) on a CdZnTe substrate (Fig. 1). Set A is Hg-vacancy p-doped through a standard technology (acceptor concentration $N_A = 2 \times 10^{16}\,\text{cm}^{-3}$), while in set B Au is used as acceptor ($N_A = 5 \times 10^{15}\,\text{cm}^{-3}$) and the number of Hg vacancies is kept low.[14,15] Both sets were fabricated as large matrices of $15\,\mu\text{m} \times 15\,\mu\text{m}$ pixels, passivated with a CdTe layer. Strong interdiffusion with the underlying HgCdTe resulted in the profile of the Cd mole fraction x reported in Fig. 2, as determined by secondary-ion mass spectroscopy (SIMS). The photodiode junctions were defined by ion implantation into the p-type layer, with maximum donor density $N_D = 10^{18}\,\text{cm}^{-3}$.

Dark current measurements were performed on HgCdTe chips hybridized to fanout circuits, with several photodiodes connected in parallel allowing the measurement of low current levels.[15] These diode fields were surrounded by rows of interconnected diodes around the perimeter, independently biased and thus acting as guard structures. In this way, the current generated outside the pixel field under consideration can be effectively siphoned off. All measurements were performed in a custom-made liquid-nitrogen evaporation cryostat where the temperature can be varied and stabilized between 80 K and 300 K. Fanout circuits were mounted into a closed cavity held at the detector temperature.

The experimental dark current density $J_{\text{dark}}(V;T)$ for set A and set B is reported in Fig. 3. For all considered temperatures, the dark current in set A is considerably higher than in set B, also for low values of reverse bias voltage V_{bias}. Moreover, a much stronger contribution of BTBT and/or II may be noticed in set A with respect to set B. The goal of the numerical investigation presented in the following section is to provide a detailed quantitative explanation of the observed differences in J_{dark} between sets A and B.*

SIMULATION OF THE LOW REVERSE BIAS REGIME

For both set A and set B, starting from the CdZnTe substrate (not included in the computational box), the simulated photodiode structures include a $7-\mu$m-thick p-type HgCdTe region, followed by a $1.5-\mu$m-thick, $10-\mu$m-wide n^-–n^+ HgCdTe region (Fig. 1), whose Cd mole fraction closely follows the experimental profile shown in Fig. 2. The n^- doping corresponds to a uniform donor density $N_D = 4 \times 10^{14}\,\text{cm}^{-3}$ while, in the topmost $0.5-\mu$m-thick n^+ region, N_D increases from $4 \times 10^{14}\,\text{cm}^{-3}$ to $10^{18}\,\text{cm}^{-3}$ with an isotropic error-function profile. The cathode is placed at the center of the n^+-doped region on the top surface and is biased at a voltage V_{bias} with respect to the reference potential of the p-doped layer contact, making

*In all $J_{\text{dark}}(V)$ characteristics reported in the present work, voltage has been given negative values when the junctions are reverse-biased. Since the bias is applied to the cathode, a reverse bias corresponds to a positive voltage with respect to the reference ground contact, connected to the p side of the diode and located far from the junction.

المنارة للاستشارات
www.manaraa.com

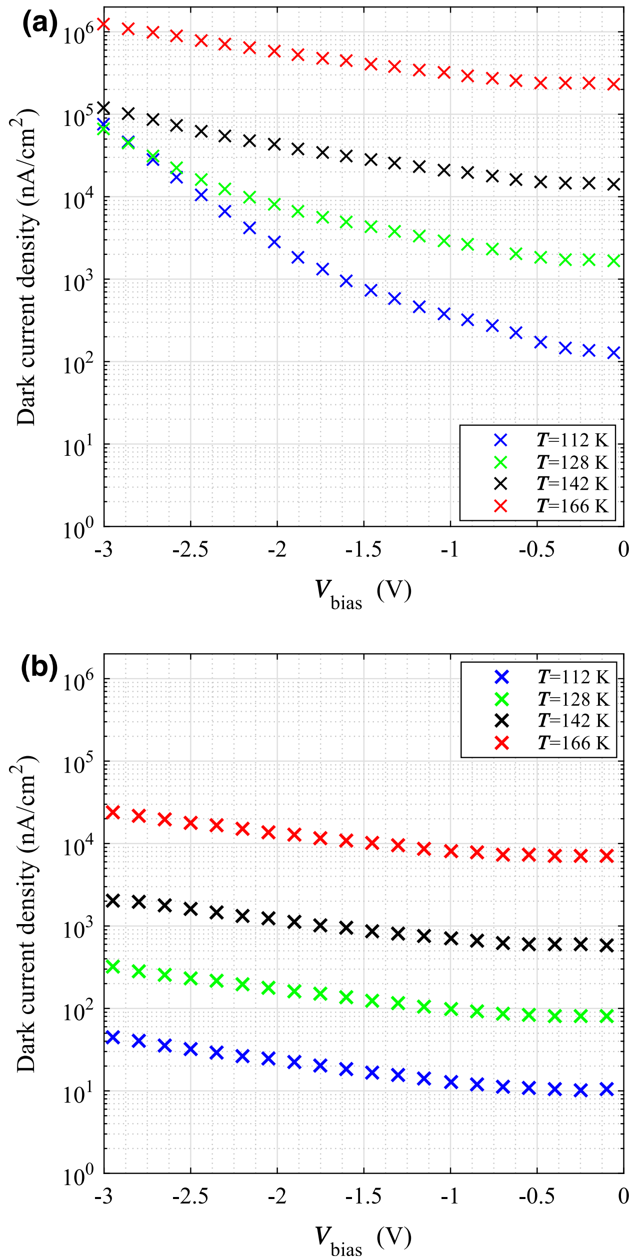

Fig. 3. Experimental $J_{\mathrm{dark}}(V;T)$ for set A (a) and set B (b).

the photodiode to operate in reverse bias. In the following, electric contacts have been considered ideally ohmic, and all electrical and optical crosstalk effects have been neglected, considering only the isolated pixel properties. The only difference between the model of the two sets of devices consists in the acceptor density N_A in the p-type absorber region, being $2 \times 10^{16}\ \mathrm{cm}^{-3}$ for set A and $5 \times 10^{15}\ \mathrm{cm}^{-3}$ for set B.

We demonstrated in a previous work[16] that 2D simulations can reliably reproduce the experimental dark currents of the photodetectors under investigation without the computational cost of a full 3D description, the only requirement being axial symmetry of the device. Therefore, our present analysis is based on the 2D numerical solution of the drift–diffusion (DD) equations using the finite-element method. Composition, doping, and temperature dependence of the electronic, transport, and optical parameters of HgCdTe are described through the models proposed in Ref. 17 (p. 1243) for the energy gap E_g, Ref. 18 (p. 1331) for the electron affinity χ, Ref. 19 for electron and hole effective masses (see also Eq. 14.6 of Ref. 4), Ref. 4 (Eq. 14.7) for electron and hole mobilities (derived from experimental measurements for Cd mole fraction between 0.2 and 0.6[20]), and Ref. 21 (Eqs. 5, 9) for radiative and Auger lifetimes, where we assume $F_{12} = 0.2$ for the overlap integral of the Bloch functions and $\gamma = 6$ for the ratio between Auger-7 and Auger-1 intrinsic lifetimes.[22,23] The simulated structures are discretized with a highly customizable meshing tool, generating a denser mesh in regions where high gradients of current density, electric field, free charge density, and material composition are expected. Fermi–Dirac statistics and incomplete dopant ionization are taken into account, with activation energies for HgCdTe alloys according to Refs. 4 and 24.

The lifetime of SRH recombination processes are modeled as[25]

$$R_{\mathrm{SRH}} = \frac{np - n_i^2}{\tau_p\left(n + n_i e^{(Et - E_{\mathrm{Fi}})/(k_B T)}\right) + \tau_n\left(p + n_i e^{-(Et - E_{\mathrm{Fi}})/(k_B T)}\right)}, \tag{1}$$

where n, p, and n_i are the electron, hole, and intrinsic density, k_B is Boltzmann's constant, T is absolute temperature, and E_t and E_{Fi} are the trap energy and intrinsic Fermi level. The lifetimes τ_n, τ_p can be expressed as[26]

$$\tau_n = \frac{1}{(N_t\sigma)_n v_{\mathrm{th},n}}, \quad \tau_p = \frac{1}{(N_t\sigma)_p v_{\mathrm{th},p}} \tag{2}$$

and depend on the local value of the product between the trap density N_t and the carrier capture cross-sections σ, and on the thermal velocity

$$v_{\mathrm{th},n} = \sqrt{\frac{3k_B T}{m_e}}, \quad v_{\mathrm{th},p} = \sqrt{\frac{3k_B T}{m_h}}, \tag{3}$$

where $m_{e,h}$ are the effective electron and hole masses. According to Ref. 7, E_t lies near the intrinsic Fermi level for n-type doping and for p-type doping with As, Cu, and Au, and is locked at $\approx$30 meV below the conduction-band edge E_c for vacancy-doped $Hg_{1-x}Cd_xTe$ with $0.2 < x < 0.5$.

The first step of the present simulation study was to reproduce the experimental dark currents at low reverse bias ($V_{\mathrm{bias}} \leq 0.5$ V) by taking into account only Auger, radiative, and SRH processes (i.e., excluding both BTBT and II). Under these assumptions, the net

المنارة للاستشارات
www.manaraa.com

Table I. Estimated SRH parameters for set A and set B

Region	$N_t\sigma$ (cm^{-1})	$E_c - E_t$ (meV)
Set A		
p	0.01	30
n^-, n^+	0.8	70
Set B		
p	0.001	30
n^-, n^+	0.0018	120

recombination rate R in the continuity equation becomes

$$R = R_{\text{Auger}} + R_{\text{Radiative}} + R_{\text{SRH}}. \tag{4}$$

The simulated dark current densities were tuned by varying only three SRH parameters: the trap energy E_t in the n section, and the products $(N_t\sigma)_{n,p}$ in the p and n regions. To reduce the complexity of the tuning process, we assumed $E_c - E_t = 30$ meV in the p section[7] of both set A and set B, since the depleted region of the photodiode extends mainly in the n^- layer, and as a result, the sensitivity of $J_{\text{dark}}(V;T)$ to the SRH parameters of the p region is almost negligible. The resulting values for $N_t\sigma$ and E_t are reported in Table I.

To estimate the relative importance of the different GR mechanisms, we also compared the dark current "components" determined by solving the DD model when each contribution to the total GR rate in Eq. 4 is considered as the only source term in the continuity equations. (Due to the nonlinearity of the DD equations, the total dark current is not expected to be the sum of the Auger, SRH, and radiative "components." Besides these GR contributions, carrier diffusion from the quasineutral to the depleted regions also plays a role,[27] although not easily separable from the others in a DD framework.) From the simulated $J_{\text{dark}}(V;T)$ characteristics, reported in Figs. 4 and 5, the following comments are in order: First, since the contributions of BTBT and II are not included, only the low-bias regime is adequately described. Second, the devices of set A are SRH-limited, given that the SRH current component dominates even at the highest temperature (Fig. 4, lower panel). In set A one can expect an additional relevant contribution by BTBT and/or II, whose extent will be investigated in the next section. In set B, neither Auger nor SRH are clearly dominant, and all the considered GR mechanisms concur to yield the observed total dark current. Assuming that the capture cross-sections are the same in the two sets and that $\sigma_n = \sigma_p$,[28] Table I suggests that in set B the trap densities in the p and n sections are, respectively, one and two orders of magnitude lower than in set A, which could be correlated to the substantial reduction of metal

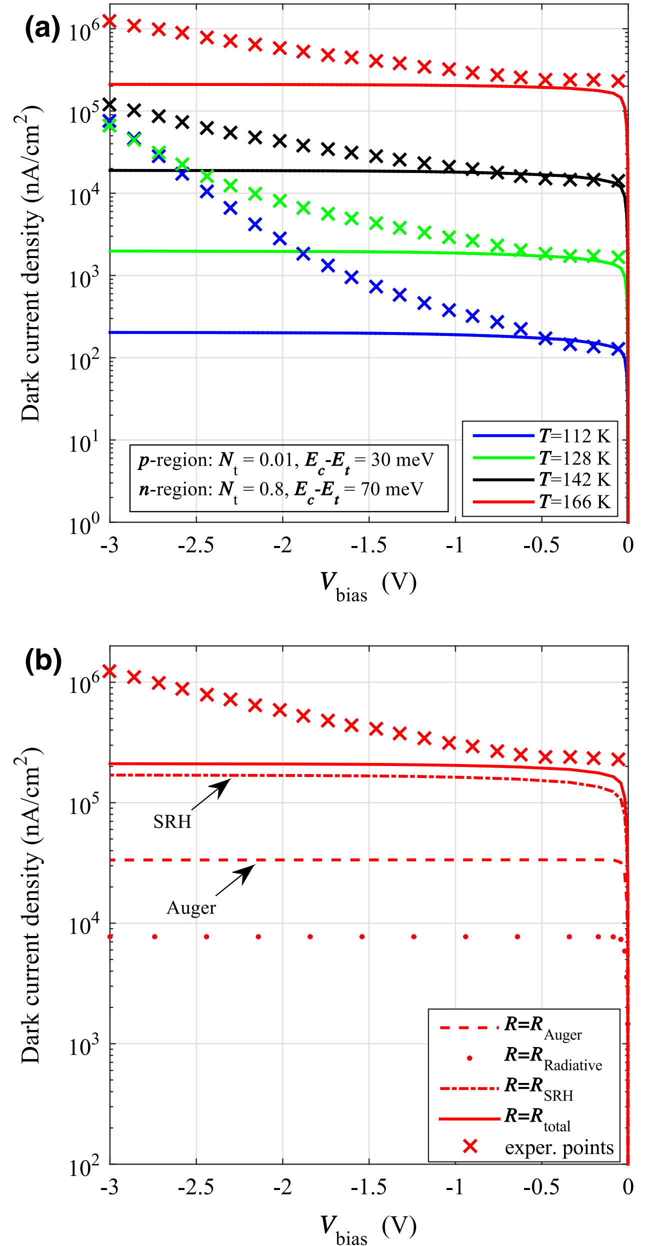

Fig. 4. Set A: simulated $J_{\text{dark}}(V;T)$ (a) and corresponding components at $T = 166$ K (b). Crosses indicate experimental values.

vacancies in set B. The estimated N_t reductions in set B bring down the SRH component by more than two orders of magnitude with respect to set A. Last, a decrease of the Auger component by one order of magnitude is observed in set B with respect to set A, which could be ascribed to the reduction of the acceptor density in the p-doped section (see "Device Fabrication and Experimental Dark Currents" section). The favorable effects of avoiding vacancy doping and reducing the doping density in the absorber region, already discussed in Ref. 7, were experimentally demonstrated in Ref. 10 for high-density vertically interconnected photodiodes

المنارة للاستشارات
www.manaraa.com

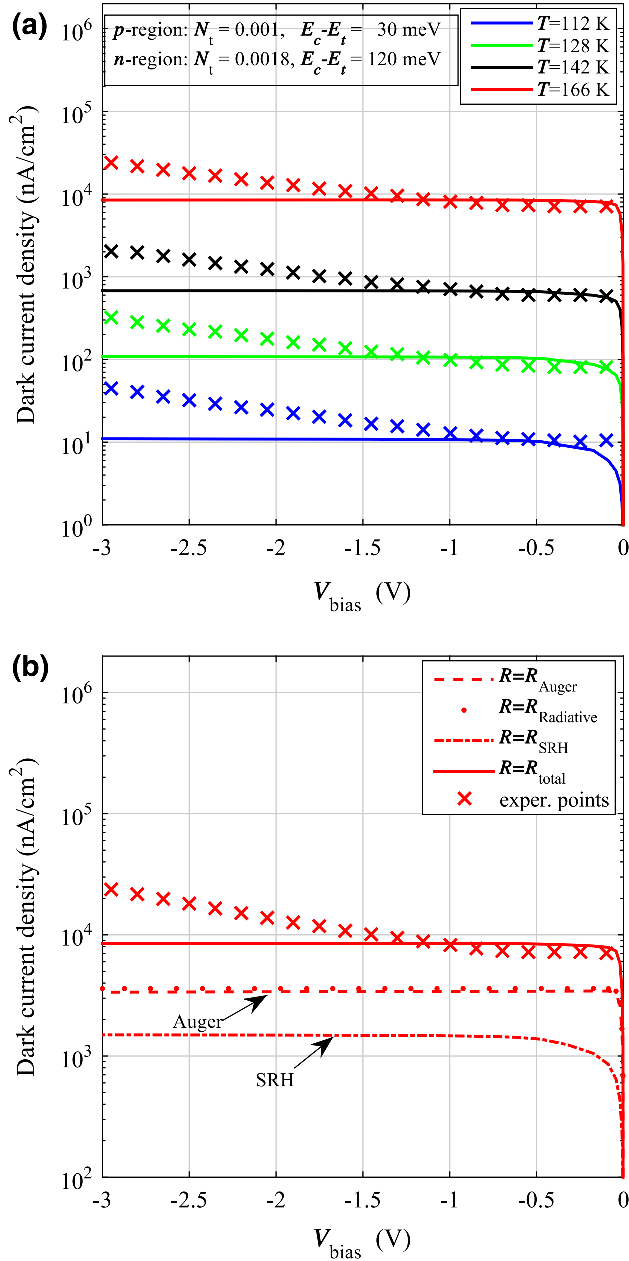

Fig. 5. Set B: simulated $J_{\rm dark}(V;T)$ (a) and corresponding components at $T = 166$ K (b). Crosses indicate experimental values.

(HDVIPs). Despite the structural differences between HDVIPs and the devices considered in the present work, the observed dark current reduction between set A and set B at 166 K is in substantial quantitative agreement with the corresponding reduction observed in Ref. 10 (Fig. 19) at about the same temperature.

SIMULATION OF THE HIGH REVERSE BIAS REGIME

The classical expression of electron BTBT is due to Kane[29]:

$$R_{\rm BTBT,\,Kane} = A\mathscr{E}^2 \exp\left(\frac{B}{\mathscr{E}}\right), \tag{5}$$

where, for parabolic barriers, the coefficients A and B are[30,31]

$$A = -\frac{q^2\sqrt{2m_{\rm e}}}{4\pi^3\hbar^2\sqrt{E_{\rm g}}}, \quad B = \frac{\pi\sqrt{m_{\rm e}E_{\rm g}^3}}{2\sqrt{2}\,q\hbar}, \tag{6}$$

q and $\hbar$ being the electron charge and the reduced Planck's constant. These expressions, as well as closely related ones derived for triangular barriers (see, e.g., Ref. 31 for a review), apply rigorously to the case of constant electric field $\mathscr{E}$ across the junction. Some authors have studied less idealized cases, accounting, e.g., for the Fermi level positions in the neutral regions[32] or considering 2D and 3D realistic junction profiles,[30,31] but the application of the corresponding solutions in device simulators is affected by serious numerical issues. With the aim of avoiding such difficulties, a different BTBT model was recently proposed for Si-based tunnel field-effect transistors[12] and p–i–n diodes.[13] According to this approach, the term $\mathscr{E}^2$ in Eq. 5 is replaced with the product $\mathscr{E}_{\rm av}^{(D-1)}\mathscr{E}$,[33] where $\mathscr{E}_{\rm av}$ is the average electric field in the depleted region and D is a dimensionless empirical parameter. Working in the Wentzel–Kramers–Brillouin (WKB) approximation, starting from the expression of the average field $\mathscr{E}_{\rm av} = E_{\rm g}/(q\,l_{\rm path})$ across the junction[33] (where $l_{\rm path}$ is the distance between the two WKB turning points, the so-called tunneling path length) and applying the charge neutrality equation, we derive the expression

$$R_{\rm BTBT} = A\,\delta^{D-1}\mathscr{E}^{\frac{D+1}{2}} \exp\left(-\frac{B}{\delta\sqrt{\mathscr{E}}}\right) \tag{7}$$

that depends on the parameters D and $\delta \approx \sqrt{2qn_{\rm iL/\varepsilon}}$, where ε is the average dielectric constant and L is the total device length. In the following, we have set $D = 1$ and we have treated δ as a fitting parameter. This formulation extends and simplifies the approach in Refs. 12, 13, and 33, overcoming some limitations of Kane's solution without introducing numerical stability issues, and in the present case allows for excellent agreement with the experimental characteristics by tuning only one parameter. The main requirement for its application is a nearly constant $\mathscr{E}$ in the depleted region. This condition is reasonably satisfied in the devices under study, as shown in Fig. 6, where the absolute value of the vertical component of the electric field $|\mathscr{E}_z|$ is reported at a bias $V_{\rm bias} = -3$ V. (The p–n^- junction is located near $z = 7\,\mu$m, and the depleted region extends mainly in the n^- side of the photodiode.)

II is customarily included in device simulations by means of a semiempirical postprocessing involving a bias-dependent gain factor $M(V)$

المنارة للاستشارات
www.manaraa.com

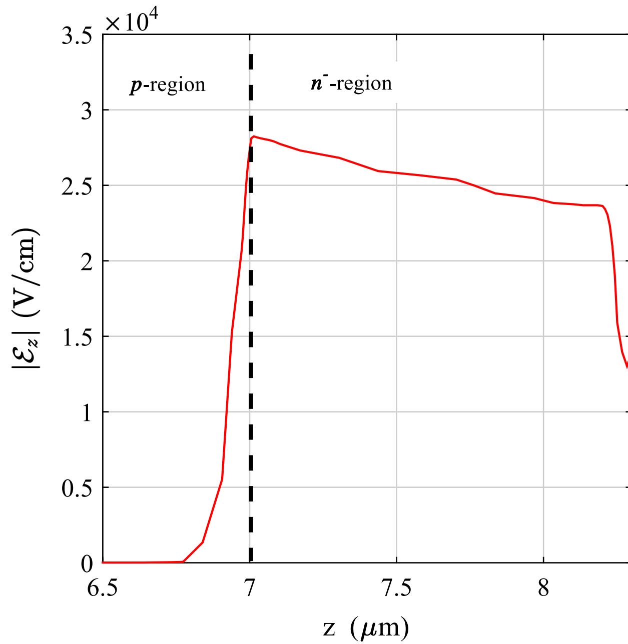

Fig. 6. Calculated vertical component of the electric field $|E_z|$ in set A near the p–n^- junction (marked with a vertical dashed line) at a bias $V_{\text{bias}} = -3$ V.

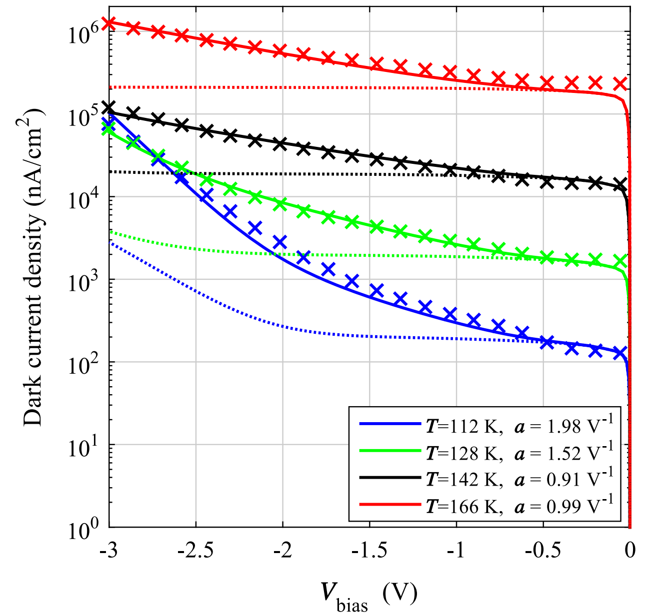

Fig. 7. Set A: simulated $J_{\text{dark}}(V;T)$ considering the contributions of Auger, SRH, and radiative GR and BTBT (dotted lines), and with the further inclusion of II (solid lines). Crosses indicate experimental values.

$$J_{\text{dark,II}}(V) = M(V) J_{\text{dark}}(V), \tag{8}$$

where $J_{\text{dark}}(V)$ is simulated taking into account all other generation mechanisms. The advantage of this approximate approach is that it avoids the very intensive computations involved in self-consistent inclusion of II in the DD model, e.g., through the Okuto–Crowell formulation.[34] One of the most popular functional forms for $M(V)$, often referred to as Beck's model, is described and theoretically justified in Ref. 35 assuming ballistic transport in the depletion layer. An alternative formulation,[36,37] successfully applied to the description of the dark current of HgCdTe avalanche photodiodes (APDs), corresponds to a gain factor having the form

$$M(V) = \exp\left[aV \exp\left(-\frac{V_{\text{th}}}{V}\right)\right] \tag{9}$$

which depends on two parameters, a and V_{th}. The authors of Ref. 36 remarked that the excess currents often attributed to BTBT at high reverse bias and to trap-assisted tunneling (TAT) at lower reverse bias could be rather ascribed in part to II. This comment also applies to the present study, because we succeeded in reproducing the experimental $J_{\text{dark}}(V;T)$ over the whole considered bias range (up to 3 V) by including II through Eq. 9, and not by including TAT.

Here, we first assigned $V_{\text{th}} = \mathscr{E}_{\text{th}} w$, where w is the width of the depleted region ($\approx 1\,\mu$m; see also Fig. 6) and $\mathscr{E}_{\text{th}} \approx 30$ kV/cm, a value considered typical for HgCdTe.[37] Then, we obtained a through an optimization process involving the experimental dark currents and the $J_{\text{dark}}(V)$ values computed by solving the DD model without II. A comparison between measurements and simulations is presented in Fig. 7 for set A, where the best agreement is observed with $\delta = 210\,\text{V}^{1/2}\text{cm}^{-1/2}$ in the BTBT model, and with the $a(T)$ values reported in the legend. The

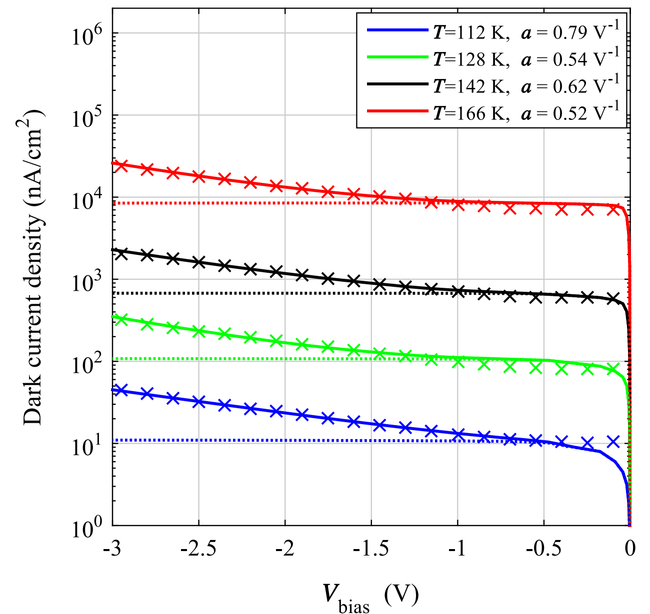

Fig. 8. Set B: simulated $J_{\text{dark}}(V;T)$ considering the contributions of Auger, SRH, and radiative GR (dotted lines), and with the further inclusion of II (solid lines). Crosses indicate experimental values. BTBT is not required to obtain satisfactory agreement with experiments.

المنارة للاستشارات
www.manaraa.com

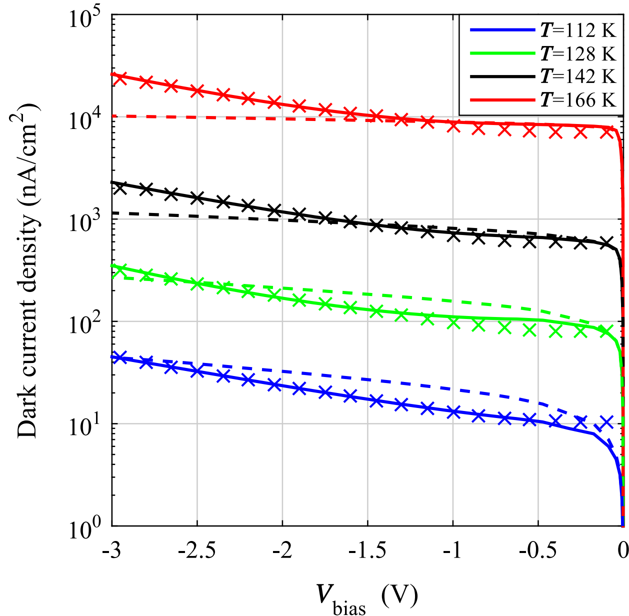

Fig. 9. Set B: simulated $J_{dark}(V;T)$ considering the contributions of Auger, SRH, and radiative GR, and either II (solid lines) or TAT (dashed lines). The T-dependence of experimental characteristics (symbols) can be reproduced with II, not with TAT.

corresponding results for set B are shown in Fig. 8, where BTBT is found to be negligible.

Concerning TAT contributions, we included them in the DD model according to Ref. 32 and observed that, at least in the considered interval of V_{bias}, they decrease rapidly with increasing temperature. On the contrary, the excess current of the devices under study is fairly insensitive to temperature (see, e.g., Figs. 7 and 8), which is considered typical of II (see Ref. 4, Sect. 14.6.3). A direct comparison between the effects of the two processes is reported for set B in Fig. 9 (similar considerations hold for set A), where it can be observed that at the highest temperature TAT has become negligible, whereas II-like contributions are important.

CONCLUSIONS

The present study supports the suggestion[7,10] that, among prerequisites to obtain HOT HgCdTe photodetectors, reduction of the Hg-vacancy density in the material is crucial due to the role of vacancies as SRH recombination centers. Also important is reducing the doping density in the absorber region and using an n-on-p architecture, due to the longer Auger-7 lifetime with respect to Auger-1. TAT processes seem to be negligible in both sets of devices under study, possibly because of the low dopant and defect densities, while II, whose contribution is sometimes neglected, has been found to be significant, becoming dominant at reverse bias larger than 1 V. Finally, BTBT has shown a correlation with the doping density of the p-type region, since it is present only in set A, where N_A is four times higher than in set B. This is likely due to the different band bending corresponding to the two doping configurations which, in turn, affects the direct tunneling path.

REFERENCES

1. M.A. Kinch, *J. Electron. Mater.* 29, 809 (2000). doi: 10.1007/s11664-000-0229-7.
2. M.B. Reine, *Proceedings of the SPIE*, vol. 4288, 2001 doi: 10.1117/12.429413.
3. A. Rogalski, *Prog. Quantum Electron.* 27, 59 (2003). doi: 10.1016/S0079-6727(02)00024-1.
4. A. Rogalski, *Infrared Detectors*, 2nd edn. (Boca Raton, FL: CRC Press, 2011).
5. M.A. Kinch, *State-of-the-Art Infrared Detector Technology* (SPIE, Bellingham, WA, 2014). doi:10.1108/eb010297.
6. T. Ashley and C.T. Elliott, *Electron. Lett.* 21, 451 (1985). doi: 10.1049/el:19850321.
7. M.A. Kinch, F. Aqariden, D. Chandra, P.K. Liao, H.F. Schaake, and H.D. Shih, *J. Electron. Mater.* 34, 880 (2005). doi:10.1007/s11664-005-0036-2.
8. M.A. Kinch, *J. Electron. Mater.* 39, 1043 (2010). doi: 10.1007/s11664-010-1087-6.
9. S. Velicu, C.H. Grein, P.Y. Emelie, A. Itsuno, J.D. Phillips, and P.S. Wijewarnasuriya, *J. Electron. Mater.* 39, 873 (2010). doi:10.1007/s11664-010-1218-0.
10. H.F. Schaake, M.A. Kinch, D. Chandra, P.K. Liao, D.F. Weirauch, C.F. Wan, and H.D. Shih, *Proceedings of the SPIE* vol. 7608, 2010. doi:10.1117/12.846254.
11. J. Wenisch, H. Bitterlich, M. Bruder, P. Fries, R. Wollrab, J. Wendler, R. Breiter, J. Ziegler, and *J. Electron. Mater.* 42, 3186 (2013). doi:10.1007/s11664-013-2757-y.
12. A.S. Verhulst, D. Leonelli, R. Rooyackers, and G. Groeseneken, *J. Appl. Phys.* 110, 024510 (2011). doi: 10.1063/1.3609064.
13. K. Ahmed, M.M.M. Elahi, and M.S. Islam, in *2012 International Conference on Informatics, Electronics and Vision (ICIEV)* (2012). doi:10.1109/ICIEV.2012.6317361.
14. J. Ziegler, D. Eich, M. Mahlein, T. Schallenberg, R. Scheibner, J. Wendler, J. Wenisch, R. Wollrab, V. Daumer, R. Rehm, F. Rutz, and M. Walther, in *Infrared Technology and Applications XXXVII*, vol. 8012, Proceedings of the SPIE, ed. by B.F. Andresen, G.F. Fulop, P.R. Norton (2011), p. 801237. doi:10.1117/12.883888.
15. R. Wollrab, W. Schirmacher, T. Schallenberg, H. Lutz, J. Wendler, and J. Ziegler, in *6th International Symposium on Optronics in Defence and Security (OPTRO 2014)* (Paris, 2014).
16. M. Vallone, M. Goano, F. Bertazzi, G. Ghione, R. Wollrab, and J. Ziegler, *J. Electron. Mater.* 43, 3070 (2014). doi: 10.1007/s11664-014-3252-9.
17. D.G. Seiler, J.R. Lowney, C.L. Litter, and M.R. LoLoee, *J. Vac. Sci. Technol. A* 8, 1237 (1990). doi:10.1116/1.576952.
18. J. Wenus, J. Rutkowski, and A. Rogalski, *IEEE Trans. Electron Devices* 48, 1326 (2001). doi:10.1109/16.930647.
19. M.H. Weiler, *Defects, (HgCd)Se, (HgCd)Te, Semiconductors and Semimetals*, 16th edn., ed. R.K. Willardson and A.C. Beer (New York: Academic, 1981), pp. 119–191.
20. J.P. Rosbeck, R.E. Starr, S.L. Price, and K.J. Riley, *J. Appl. Phys.* 53, 6430 (1982). doi:10.1063/1.331516.
21. V.C. Lopes, A.J. Syllaios, and M.C. Chen, *Semicond. Sci. Tech.* 8, 824 (1993). doi:10.1088/0268-1242/8/6S/005.
22. T. Casselman, *J. Appl. Phys.* 52, 848 (1981). doi: 10.1063/1.328426.
23. F. Bertazzi, M. Goano, and E. Bellotti, *J. Electron. Mater.* 40, 1663 (2011). doi:10.1007/s11664-011-1638-5.
24. P. Capper and J. Garland *Mercury Cadmium Telluride. Growth, Properties and Applications* (Chichester, UK: Wiley, 2011).
25. W. Shockley and W.T. Read, *Phys. Rev.* 87, 835 (1952). doi: 10.1103/PhysRev.87.835.
26. S.M. Sze and K.K. Ng, *Physics of Semiconductor Devices*, 3rd edn. (Wiley, Hoboken, NJ, 2007).

المنارة للاستشارات
www.manaraa.com

27. M.A. Kinch, *J. Electron. Mater.* (2015, online). doi:10.1007/s11664-015-3717-5.
28. S. Krishnamurthy, M.A. Berding, Z.G. Yu, C.H. Swartz, T.H. Myers, D.D. Edwall, and R. DeWames, *J. Electron. Mater.* 34, 873 (2005). doi:10.1007/s11664-005-0035-3.
29. E.O. Kane, *J. Appl. Phys.* 32, 83 (1961). doi:10.1063/1.1735965.
30. R. Adar, *IEEE Trans. Electron Devices* 39, 976 (1992). doi:10.1109/16.127459.
31. K. Jóźwikowski, M. Kopytko, A. Rogalski, and A. Jóźwikowska, *J. Appl. Phys.* 108, 074519 (2010). doi:10.1063/1.3483926.
32. G.A.M. Hurkx, D.B.M. Klaassen, and M.P.G. Knuvers, *IEEE Trans. Electron Devices* 39, 331 (1992). doi:10.1109/16.121690.
33. W. Vandenberghe, B. Sorée, W. Magnus, and M.V. Fischetti, *J. Appl. Phys.* 109, 124503 (2011). doi:10.1063/1.3595672.
34. Y. Okuto and C.R. Crowell, *Phys. Rev. B* 6, 3076 (1972). doi:10.1103/PhysRevB.6.3076.
35. M.A. Kinch, J.D. Beck, C.F. Wan, F. Ma, and J. Campbell, *J. Electron. Mater.* 33, 630 (2004). doi:10.1007/s11664-004-0058-1.
36. C.T. Elliott, N.T. Gordon, R.S. Hall, and G. Crimes, *J. Vac. Sci. Technol. A* 8, 1251 (1990). doi:10.1116/1.576954.
37. J. Rothman, L. Mollard, S. Goût, L. Bonnefond, and J. Wlassow, *J. Electron. Mater.* 40, 1757 (2011). doi:10.1007/s11664-011-1679-9.

المنارة للاستشارات

www.manaraa.com

Reproduced with permission of the copyright owner. Further reproduction prohibited without permission.

للاستشارات المنارة

www.manaraa.com